nature physics

Article

https://doi.org/10.1038/s41567-023-02053-z

Flat band separation and robust spin Berry curvature in bilayer kagome metals

Received: 1 November 2022

Accepted: 5 April 2023

Published online: 18 May 2023

Check for updates

Domenico Di Sante[1,2] ✉, Chiara Bigi[3], Philipp Eck[4], Stefan Enzner[4], Armando Consiglio[4], Ganesh Pokharel[5], Pietro Carrara[6,7], Pasquale Orgiani[8], Vincent Polewczyk[8], Jun Fujii[7], Phil D. C. King[3], Ivana Vobornik[7], Giorgio Rossi[6,7], Ilija Zeljkovic[9], Stephen D. Wilson[5], Ronny Thomale[4], Giorgio Sangiovanni[4] ✉, Giancarlo Panaccione[7] ✉ & Federico Mazzola[7,10] ✉

Kagome materials have emerged as a setting for emergent electronic phenomena that encompass different aspects of symmetry and topology. It is debated whether the XV_6Sn_6 kagome family (where X is a rare-earth element), a recently discovered family of bilayer kagome metals, hosts a topologically non-trivial ground state resulting from the opening of spin–orbit coupling gaps. These states would carry a finite spin Berry curvature, and topological surface states. Here we investigate the spin and electronic structure of the XV_6Sn_6 kagome family. We obtain evidence for a finite spin Berry curvature contribution at the centre of the Brillouin zone, where the nearly flat band detaches from the dispersing Dirac band because of spin–orbit coupling. In addition, the spin Berry curvature is further investigated in the charge density wave regime of ScV_6Sn_6 and it is found to be robust against the onset of the temperature-driven ordered phase. Utilizing the sensitivity of angle-resolved photoemission spectroscopy to the spin and orbital angular momentum, our work unveils the spin Berry curvature of topological kagome metals and helps to define its spectroscopic fingerprint.

Electrons on a kagome lattice constitute a pre-eminently suited scenario for exotic quantum phenomena at all coupling scales: within the Mott limit, it is the established paradigmatic setting for spin liquids and other aspects of frustrated magnets[1]. For symmetric metallic states or itinerant magnets, the diversity of dispersing kagome signatures such as Dirac cones, flat bands and van Hove singularities enable a plethora of correlated electron phenomena from topological band formation and symmetry breaking to be unlocked[2–14].

The family of XV_6Sn_6 kagome materials, where X is a rare-earth element, belongs to a new series (hereafter dubbed the '166' family) that has been predicted to host electronic states with non-trivial topology. In particular, not only are the surface states that appear at natural cleavage planes of the crystals theoretically conceived to have a non-trivial origin[15,16], but also the correlated flat band naturally arising from the kagome geometry[17] is characterized by a non-zero $\mathbb{Z}_2$ Kane–Mele invariant for the action of spin–orbit coupling (SOC)[18–24].

[1]Department of Physics and Astronomy, University of Bologna, Bologna, Italy. [2]Center for Computational Quantum Physics, Flatiron Institute, New York, NY, USA. [3]School of Physics and Astronomy, University of St Andrews, St Andrews, UK. [4]Institut für Theoretische Physik und Astrophysik and Würzburg-Dresden Cluster of Excellence ct.qmat, Universität Würzburg, Würzburg, Germany. [5]Materials Department, University of California Santa Barbara, Santa Barbara, CA, USA. [6]Dipartimento di Fisica, Universitá degli Studi di Milano, Milano, Italy. [7]Istituto Officina dei Materiali, Consiglio Nazionale delle Ricerche, Trieste, Italy. [8]CNR-IOM TASC Laboratory, Area Science Park, Trieste, Italy. [9]Department of Physics, Boston College, Chestnut Hill, MA, USA. [10]Department of Molecular Sciences and Nanosystems, Ca' Foscari University of Venice, Venice, Italy. ✉e-mail: domenico.disante@unibo.it; sangiovanni@physik.uni-wuerzburg.de; panaccione@iom.cnr.it; federico.mazzola@unive.it

If the onsite energy of such a separated flat band could be controlled, one could trigger new topological phases with potential applications in spintronics and non-volatile electronics[25–29]. Therefore, uncovering the non-trivial topological character of such a flat band would be a true milestone in the field of condensed matter physics.

The direct experimental observation of non-trivial topological properties in 166 kagome metals remains an open challenge. Although transport is unable to probe correlated flat band states below the Fermi level E_F or isolate topological surface states[10,11,30–36], in angle-resolved photoemission spectroscopy (ARPES) there are tantalizing hints that these states exist. Crucially, measurements of the spin degree of freedom are missing; when ARPES has been able to detect the surface states manifold and the flat bands in XV_6Sn_6 systems[15,16,37], the lack of measurements for the spin degree of freedom and the action on it of time-reversal symmetry hinder the conclusive proof of their topological nature.

Here we provide the spectroscopic evidence of the non-trivial topology in the 166′ kagome family. We use spin-ARPES and density functional theory (DFT) calculations to determine the electronic structure of these systems resolved in energy, momentum and spin. We not only find a net spin polarization of the surface states in the prototypical compound TbV_6Sn_6, but we ultimately demonstrate the non-trivial topology of the gap between the dispersive Dirac band and the nearly flat band arising from the kagome geometry. Such a gap is a common feature of all kagome lattices with non-zero SOC, and its nature is believed to be topological, yet its demonstration has been elusive until now[10,11,35,38]. Notably, we detect a finite spin Berry curvature in kagome metals, and by systematically studying the whole series of $(Tb,Ho,Sc)V_6Sn_6$ compounds, we also demonstrate its resilience against the onset of a charge ordered phase, which is a distinctive feature of many recently discovered kagome metals[9,39,40]. As well as unveiling the interplay between many-body electronic states and topology in this class of materials, our work provides experimental measurements of a spin Berry curvature in real quantum systems. Indeed, the detection of energy- and momentum-resolved finite Berry curvature signals was hitherto limited to cold atom experiments, which unveiled the deep relationship between topology and flatness in optical lattices[41]. Furthermore, in that context, flat bands serve as a platform for emergent correlated phases and their simplicity can advance the understanding of the physics that occurs in argon ice, Landau levels and twisted Van der Waals bilayers[42]. Here we extend this context to real solid-state systems.

TbV_6Sn_6 (Fig. 1a) is a kagome system belonging to the 166 family of rare-earth kagome metals, along with GdV_6Sn_6 and HoV_6Sn_6 (refs. 5,37,43,44). It exhibits a uniaxial ferromagnetic transition at 4.1 K with a substantial anisotropy in the magnetic susceptibility, suggesting a ferromagnetic alignment of Tb^{3+} 4*f* moments perpendicular to the V kagome layers[44]. The DFT bulk electronic band structure is shown in Fig. 1b. It is characterized by prominent features hinting at a non-trivial topology. Dirac-like dispersions appear at the K points of the Brillouin zone (BZ) and contribute to the metallic character of the material. In addition, two flat bands are visible below and above the chemical potential, as highlighted by the yellow colour proportional to the band *n*- and momentum **k**-resolved density of states $\rho_{n\mathbf{k}} \approx 1/v_{n\mathbf{k}}$, where $v_{n\mathbf{k}}$ represents the electronic velocity. Both the Dirac cones and the flat band around −1 eV are spectroscopically detectable by ARPES owing to their occupied character. As shown in Fig. 1c, which shows enlargements of the red rectangles (1) and (2) of Fig. 1b, SOC opens gaps at the Dirac cones. The SOC permits direct gaps between bands throughout the BZ, which in turn allows the topological invariant $\mathbb{Z}_2$ for the occupied bands to be defined using parity products at time-reversal invariant momenta[45]. As for GdV_6Sn_6 (refs. 15,16), we find $\mathbb{Z}_2 = 1$ for the bands around the Fermi level. We also highlight that, in the absence of SOC, the Dirac cones carry a finite Chern number $\mathcal{C}$, and are the source and sink of finite Berry curvature $\Omega(\mathbf{k})$, resulting in topologically protected arcs on the surface of this class of materials, as Fig. 1g shows.

On cleavage, two terminations are possible, namely a Sn-terminated and a mixed V/Sn-terminated surface plane, with the latter being characterized by V atoms arranged into a kagome pattern. To determine the type of termination, we acquired the Sn core levels alongside the ARPES, finding good agreement with previous works on the sister compound GdV_6Sn_6 (ref. 37). Specifically, as shown in Fig. 1d, the Sn termination exhibits the presence of two extra peaks at lower binding energies in the Sn 4*d* core levels, compatible with the corresponding Sn-derived surface components. The kagome termination, on the other hand, shows a substantially different line shape, featuring an asymmetric profile and a shift of about 0.43 eV towards higher binding energy values. These differences are attributed to the different local atomic environment present at the two surfaces[37]. The measured Fermi surfaces (Fig. 1e,f) for both terminations agree well with the calculated ones (Supplementary Fig. 2) and the typical kagome motif of corner-sharing triangles is also recognizable in reciprocal space.

The surface states at the kagome termination have minimal separation from the bulk continuum[15,16]. This makes their spin-resolved measurements challenging, since the bulk contribution is intense and makes the spin-polarized signal too weak to be observed (see also Supplementary Fig. 3 for additional spectra). However, the Sn-terminated surface features well-separated surface states, which allow the spin-ARPES experiments to be performed more easily, offering the perfect playground to investigate the topological properties of this system. We will focus on this termination when discussing the topological character of the surface states of TbV_6Sn_6. In contrast, the correlated flat band topology is not termination-dependent. Such a band, in fact, is a feature inherent to the bulk kagome geometry, making this study of broad interest for kagome lattices in general and offering a comparative parallel case study for other systems. In addition, to determine the topology of the gap between the Dirac state and the flat band, the experimental measurement of the spin Berry curvature is essential, because all the electronic states are spin degenerate, and thus inaccessible by standard spin-ARPES.

The high-resolution electronic structure of the Sn termination is shown in Fig. 2. By using both linear vertical and horizontal light polarization (E_s and E_p, respectively; see also the experimental setting in Fig. 2a), we detect a plethora of interesting electron features, as shown in Fig. 2b,c; multiple Dirac dispersions, van Hove singularities and the correlated flat band, which are a hallmark of kagome materials, are well identified. In particular, the van Hove singularities are located slightly above the Fermi energy and at about −0.4 eV (labelled VH_1 and VH_2 in Fig. 2f) and are visible in both theory and experiment. In addition, the Dirac cones form at the K point at binding energies of −1.5 eV (D_1) and −0.3 eV (D_2) (Fig. 2b,f). The latter set of bands evolves symmetrically across the BZ with a quadratic minimum (Fig. 2b) at the zone centre. According to a basic first-nearest-neighbour tight-binding calculation (see also Fig. 4a), such a quadratic minimum is pinned to the flat band. We clearly detect both features in Fig. 2d and the relative energy distribution curves (the blue and green curves) in Fig. 2e. We also notice that the flat band is only visible with E_s polarized light, while the quadratic minimum intensity disappears at the zone centre because of the photoemission matrix elements. Nonetheless, the quadratic minimum is well identified in the energy distribution curve acquired with E_p polarization (blue curve), for which, instead, the flat band is not visible. Thus, the combination of E_s and E_p allows us to visualize both the quadratic minimum and the flat band, and to estimate the SOC-induced gap between them to be ~60 meV. Importantly, the presence of SOC mixes the orbital character across the opening point at Γ, and induces a finite spin Berry curvature (see again Fig. 4a and further discussion).

Close to the Fermi level, our ARPES measurements and DFT calculations enable the investigation of the topological nature of the 166 family. We focus on the surface states originating from the multiple gapped Dirac cones described in Fig. 1b,c. In previous literature, theoretical works have attempted a topological classification of the $\mathbb{Z}_2$

https://doi.org/10.1038/s41567-023-02053-z

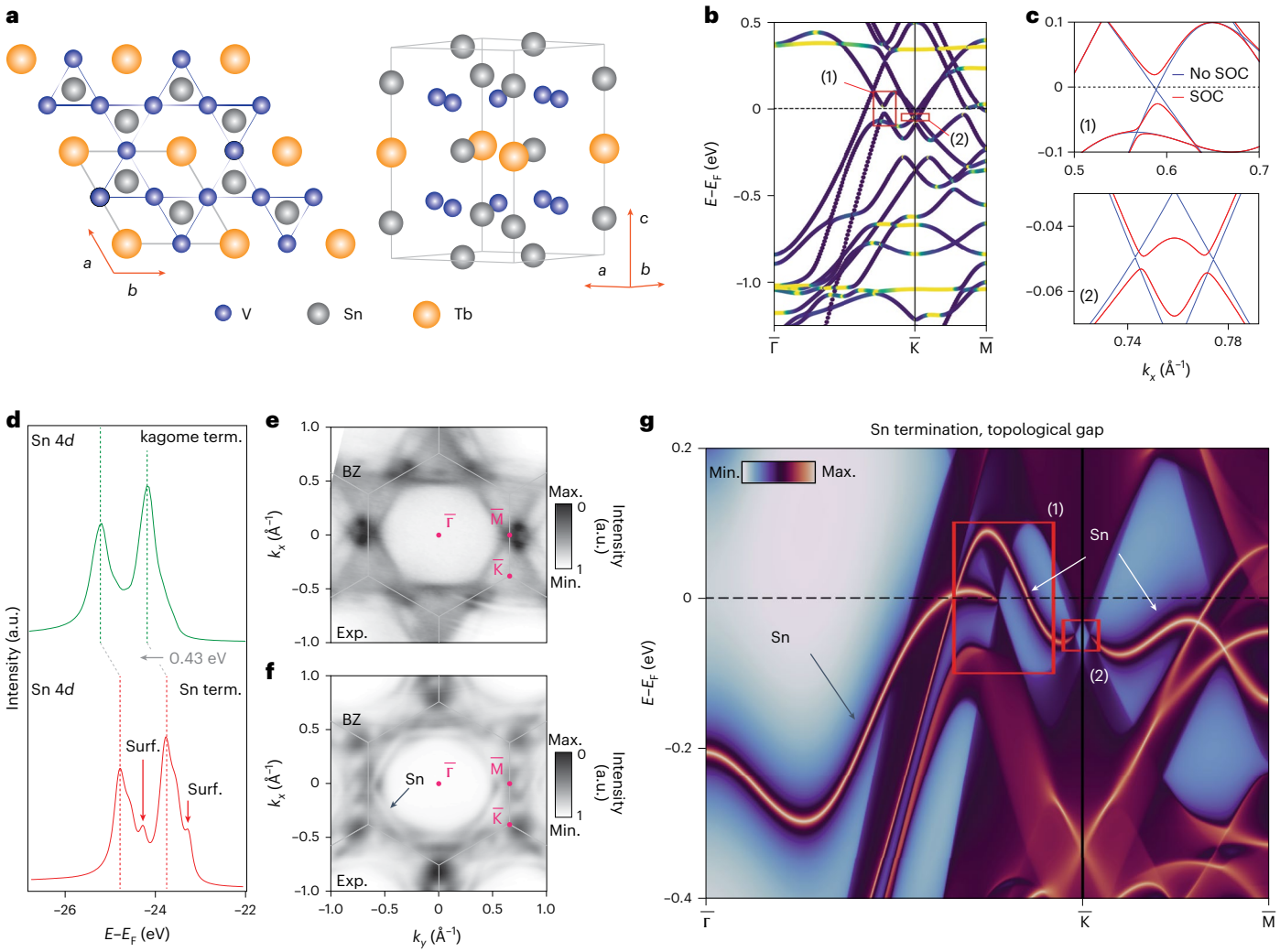

Fig. 1 | Crystal structure, bulk electronic properties and surface terminations of TbV_6Sn_6 kagome metal. a, Crystal structure of TbV_6Sn_6 showing top and side views of the unit cell. **b**, Bulk electronic structure along the Γ–K–M direction in the presence of SOC. The electronic states are coloured by the band and momentum-resolved density of states, with yellow highlighting a large contribution. **c**, Enlargement of the red boxes (1) and (2) in **b**. Red and blue bands refer to calculations with and without SOC, respectively. **d**, Sn 4*d* core level spectroscopy for the kagome-terminated (term.) (green) and Sn-terminated (red) surface (surf.) of TbV_6Sn_6. **e**,**f**, ARPES Fermi surfaces for the kagome (**e**) and Sn (**f**) termination of TbV_6Sn_6, respectively. **g**, Spectral function of the (001) surface Green's function for the Sn termination in the absence of SOC. Boxes (1) and (2) refer to those in **b**.

invariant of the surface states across the BZ. According to Hu et al.[16], topological surface states in GdV_6Sn_6 are expected to cover a significant portion of the BZ, bridging a large bulk gap across Γ. In contrast to these data, our ARPES spectra in Fig. 2f does not reveal any surface states through the Fermi level around the Γ point, probably due to a different chemical potential in TbV_6Sn_6, which pushes them into the unoccupied region of the electronic density of states. This observation is consistent with our slab calculation of the electronic structure in Fig. 2g, which, differently from the spectrum in Fig. 1g, fully accounts for the structural relaxation of atoms at the Sn-terminated surface, where these states are present. They are primarily unoccupied, but a portion of them bridges the gap below the Fermi energy along the $\bar{\Gamma}$–$\bar{M}$ line. We also notice that in Fig. 2g these surface states form a small electron pocket close to the centre of the BZ. This pocket is absent in ARPES. Nonetheless, the presence of these surface states close to the K point is enforced by topology, because they originate as Fermi arcs from the Dirac cones. Therefore, in this region, we will seek the signature of the spin-polarized feature in ARPES, because these states are accessible there.

To experimentally verify this, we first calculated the expected spin texture of the Sn surface states. The calculated spin-resolved electronic structure is shown in Fig. 3a. We found that the spin component along *y* S_y gives the most significant and only non-zero contribution along the $\bar{\Gamma}$–$\bar{K}$–$\bar{M}$ k_x direction (see Supplementary Fig. 9 for the spin components along *x* S_x and and *z* S_z components). This result demonstrates the spin-momentum locking of the spin texture and its non-trivial origin. Using the ARPES analyser's deflectors, we measured the spin-ARPES signal along $\bar{\Gamma}$–$\bar{K}$–$\bar{M}$ direction at specific momenta for both positive and negative **k** values (the coloured vertical bars in Fig. 3a). In this way, not only can the theoretical predictions be proved, but the time-reversal symmetry constraint can also be verified by keeping the same matrix elements. The spin-ARPES data for S_y are shown in Fig. 3b–e (see Supplementary Information for details about data normalization). A clear spin-resolved signal in the proximity of the Fermi level confirms a non-vanishing spin polarization typical of spin-polarized states. In addition, the spin sign reverses with the momentum **k**, guaranteeing the time-reversal symmetry of the system. This important aspect is also compatible with the sample being well above the magnetic transition temperature (the measurements were indeed performed at 77 K). In addition, the Tb 4*f* levels are well separated from the near-Fermi energy region and do not

https://doi.org/10.1038/s41567-023-02053-z

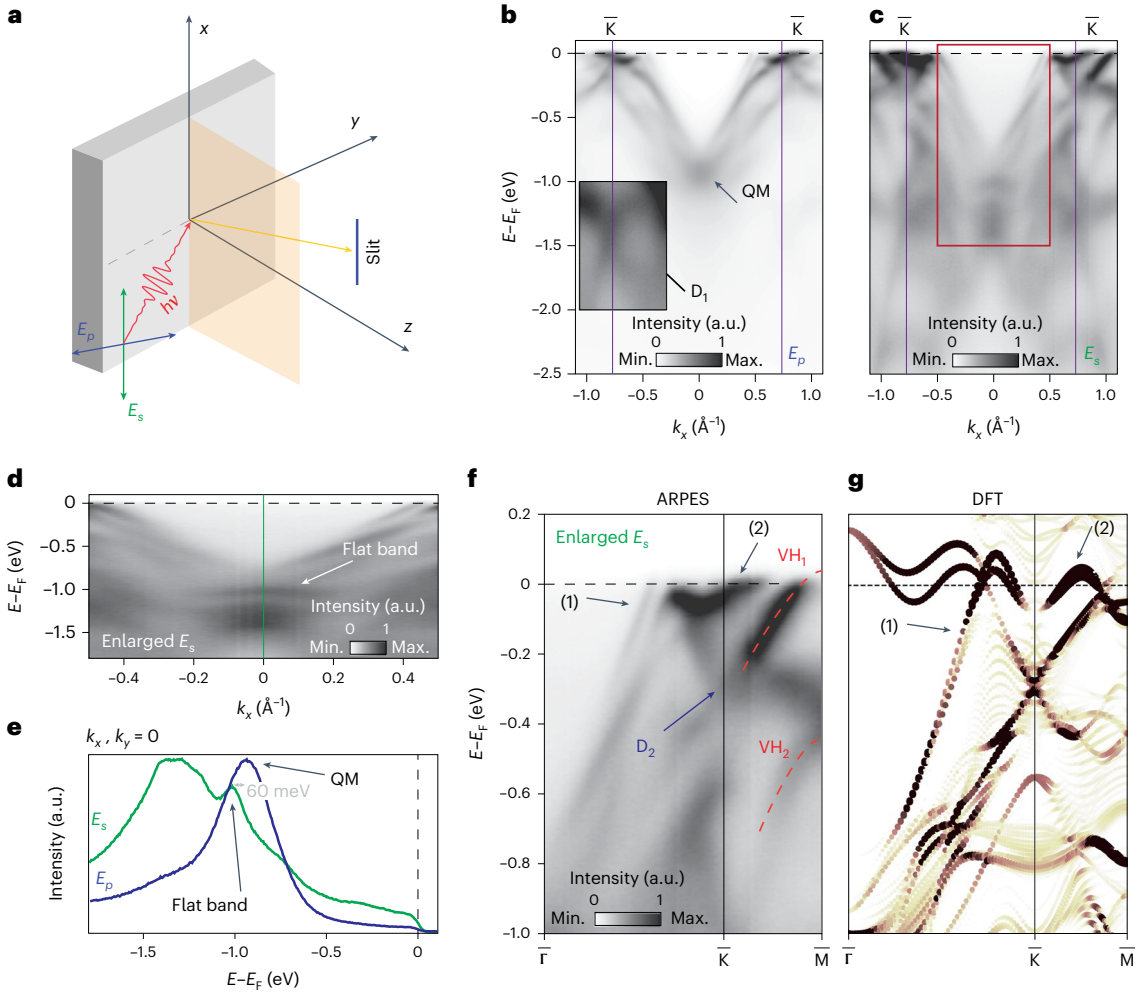

Fig. 2 | Spectroscopy of the surface states and of the flat band. a, Experimental ARPES setting of linear vertical (E_p) and horizontal (E_s) light polarizations (h is the Planck constant and v the frequency of light). E_s is fully in-plane and parallel to the x axis. E_p has an incidence angle of 45°, and thus has 50% of the out-of-plane contribution and 50% of the in-plane contribution parallel to the y axis. **b**,**c**, ARPES spectra recorded with E_p (**b**) and E_s (**c**) lights. QM, quadratic minimum. **d**, Enlarged view of the red box in **c** highlighting the dispersion of the flat band around the Γ point at approximately −1 eV of binding energy. **e**, Energy distribution curve along the green line of **d** collected with E_s polarization (green curve) and for E_p polarization (blue curve). The former shows the flat band position for $k_{x,y} = 0$; the latter instead has prominent intensity corresponding to the quadratic minimum, as is also visible in **b** and **c**. **f**, Enlargement of the ARPES data in the proximity of the Fermi level showing the most intense Sn-derived surface states (indicated by arrows labelled (1) and (2)) and also the van Hove singularities VH_1 and VH_2 at the M point, with the maximum of VH_1 slightly above the Fermi level. **g**, First-principles electronic structure of a finite slab of TbV_6Sn_6 on structural relaxation of the atoms at the Sn termination. As in **f**, arrows labelled (1) and (2) indicate the most intense Sn-derived surface states.

hybridize significantly with the measured surface states (see also Supplementary Fig. 4).

The energy distribution curves of Fig. 3b–e unambiguously demonstrate the spin-polarized character of the surface states in TbV_6Sn_6. In Supplementary Fig. 5, a thicker energy distribution curve map is also available for completeness. We notice that of the full set of states present in the DFT calculations, we are only able to resolve those that are well separated from the bulk electronic structure and that appear more prominent in intensity within the gap, which still provides sufficient evidence for the spin-momentum locking expected for these spectrocopic features. As such, this makes our finding relevant within the framework of transport experiments in kagome lattices[9,31,46–51].

Standard spin-ARPES, on the other hand, cannot be used to prove the topological character of the gap between the correlated kagome flat band and the quadratic minimum because those bands are spin degenerate. Theoretically, one can access the topological character of the gap by calculating the spin Berry curvature of this system. The Chern number $\mathcal{C}$ of each band forming such a gap is identically zero owing to the combined action of inversion (which gives $\Omega_{n\uparrow}(\mathbf{k}) = \Omega_{n\uparrow}(-\mathbf{k})$ for the Berry curvature) and time-reversal symmetry (which enforces $\Omega_{n\uparrow}(\mathbf{k}) = \Omega_{n\downarrow}(-\mathbf{k})$). Nonetheless, one can expect a finite spin Berry curvature $\Omega_z^{S_z}(\mathbf{k})$ due to the action of SOC. At the level of a simple first-nearest-neighbour tight-binding model with hopping amplitude t, SOC opens a gap at the Γ point between the parabolic dispersion from the Dirac band (1) and the flat band (2), as shown in Fig. 4a. The opening of a gap is in general associated with the appearance of a finite dispersion for the flat band[18,52], and SOC can be thought of as a perturbation breaking the real-space topology that protects the band touching in generic frustrated hopping models[53]. In modern language, kagome spectra without a mathematically flat band cannot be derived as one of the two isospectral partners of a supersymmetric bipartite graph with finite Witten index[54]. As a result, the electronic states around the opened gap feature a finite spin Berry curvature, leading to a non-trivial spin-Chern number for the weakly dispersing flat band itself. Similar conclusions hold also for TbV_6Sn_6, as shown in Fig. 4b (top panel), even though the band structure is much more complex

https://doi.org/10.1038/s41567-023-02053-z

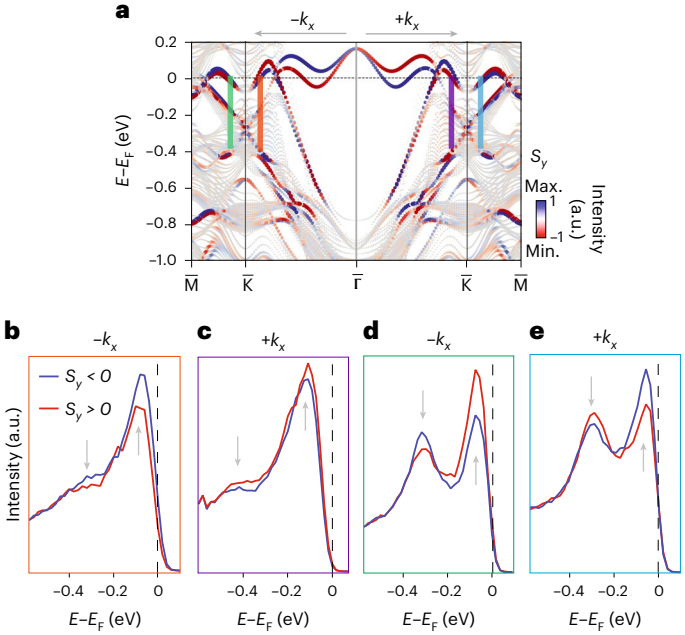

Fig. 3 | Spin texture of topological surface states. a, First-principles electronic structure of the Sn termination of a finite slab of TbV_6Sn_6 where the electronic states are coloured by their S_y character. **b**–**e**, S_y spin-resolved ARPES energy distribution curves at the specific momenta highlighted in **a** by the coloured vertical bars (orange (**b**), purple (**c**), green (**d**) and blue (**e**)). The grey arrows refer to the energy regions where a finite spin asymmetry for the surface states is measured.

than the simplified picture shown by the tight-binding model (notice, for instance, the presence of a spectator band carrying vanishing spin Berry curvature at Γ). In addition, away from the flat band region around the Γ point, our theoretical calculations reveal enhanced spin Berry curvature at every SOC-induced gap avoided crossing between two spin-degenerate bands.

Schüler et al.[55] recently proposed a methodology based on circular dichroism (CD) and spin-ARPES to directly address a signal proportional to the spin Berry curvature $\Omega_z^{S_z}(\mathbf{k})$ of quantum materials, thus allowing us to disentangle the trivial and non-trivial topologies. CD has already been used in ARPES experiments to obtain information about the Berry curvature[56,57]. However, the presence of inversion symmetry and SOC in TbV_6Sn_6 requires separating the two spin channels, that is, $\pm S_z$, as we show in Fig. 4c,d. In addition, to ensure that any geometrical contribution will not artificially alter our measurements, we measure the CD at the BZ centre, where the geometrical contribution is exactly zero, and so it is the spin-integrated dichroic signal. Being at the BZ centre also has the advantage that this point is time-reversal symmetric; thus, we are able to detect a signal reversal for the plus and minus components of the spin. Our measurements, shown in Fig. 4e, demonstrate a substantial non-zero signal for each spin species of the quadratic minimum (approximately −1 eV) and for electronic bands at slightly higher binding energies where also a finite spin Berry curvature appears as a result of SOC (greater than approximately −1.2 eV), with a reversal between spin up and down channels (red and blue, respectively). The spin Berry curvature contribution at −1 eV comes from the quadratic minimum and this can be understood by looking at the spin-integrated CD ARPES (Supplementary Fig. 1) when compared to the measurements performed with E_s and E_p light polarization: the circular light has matrix elements similar to E_p, and thus the CD ARPES results in a vanishing spectral weight for the flat band and a clear signal for the quadratic minimum, at the BZ centre. Thus, we can attribute the strong intensity peaked at −1 eV of Fig. 4e to the spin Berry curvature of the quadratic minimum. Similar conclusions can also be drawn for HoV_6Sn_6, as we experimentally show in Fig. 4f,g. It is worth stressing that by changing the photon energy we were not able to resolve the flat band by using circularly polarized light; by contrast, in this experimental configuration, the quadratic minimum was the only resolved feature. This result agrees with our calculations of Fig. 4b (top panel) that suggest a finite spin Berry curvature contribution around the SOC gap for the visible band (1) forming the quadratic minimum. Our analysis is proof of a topological gap in a kagome metal. In addition, our CD measurements in Fig. 4e unveil a large signal at energies below the flat band region. This result is again supported by our first-principles calculations of $\Omega_z^{S_z}(\mathbf{k})$, as we show in Fig. 4b (bottom panel), where the electronic states around −1.3 eV and −1.4 eV are characterized by an enhanced spin Berry curvature.

Kagome metals are also getting much attention since they represent the perfect playground for several intertwined many-body orders[9]. The unconventional charge density wave (CDW) is one of these. Its origin, whether it arises from electron–phonon coupling, electron–electron interactions or a combination thereof, is still a matter of debate. Differently from TbV_6Sn_6 and HoV_6Sn_6, ScV_6Sn_6 shows a CDW phase below the temperature $T_{CDW} \approx 92$ K, characterized by a distinctly different structural mode than that observed in the archetypal AV_3Sb_5 (A = K, Rb, Cs) compounds[39] and FeGe (ref. 40). In Fig. 4h,i we present our spin-resolved CD results for ScV_6Sn_6 at low temperature, that is, inside the charge ordered phase, whereas in Supplementary Fig. 10 we show that, in addition to an increase in the noise level due to thermal broadening, the aforementioned CD results are identical above and below T_{CDW}. Clearly, around −1 eV, we see a net spin asymmetry that reverses sign when the light polarization is changed. This result unambiguously demonstrates that the spin Berry curvature is robust against the onset of the ordered phase and that the SOC-induced energy scale associated with the appearance of a finite spin Berry curvature is larger than that correlated to the CDW symmetry breaking. Interestingly, our first-principles calculations, shown in Supplementary Fig. 8, reveal that, on unfolding the band structure of the distorted ScV_6Sn_6 onto the primitive unit cell, the CDW distortion affects only marginally the electronic properties. This is in striking contrast to the effect of the CDW order in AV_3Sb_5 compounds, where sizable band gaps open around the chemical potential[58,59].

In conclusion, we have demonstrated the topological nature of XV_6Sn_6 kagome metals by exploiting the combination of spin-ARPES and DFT calculations and leveraging the sensitivity at the multiple energy scales relevant to kagome systems. As well as unveiling a net spin polarization of the surface states of TbV_6Sn_6, which originates from the non-trivial $\mathbb{Z}_2$ invariant of the SOC-induced bulk gaps close to the Fermi energy, we have crucially shown that the correlated flat band region is characterized by a finite spin Berry curvature, establishing its topological character. In addition, we have reported the resilience of the non-trivial topology against the onset of the charge ordered phase in ScV_6Sn_6, revealing its ubiquitous nature across the series. This will motivate the investigation of the spin Berry curvature in other kagome metals as well, such as AV_3Sb_5 and FeGe, where a non-trivial flat band separation has also been predicted and in which the charge order has a strong effect on the electronic properties. Within a more general perspective, our work constitutes evidence of the multidimensional topological nature, that is, from surface to bulk states, of the 166 kagome family. It ultimately establishes these systems as a new domain for correlated topological metallicity with a non-trivial spin Berry curvature of the wave function manifold.

Online content

Any methods, additional references, Nature Portfolio reporting summaries, source data, extended data, supplementary information, acknowledgements, peer review information; details of author contributions and competing interests; and statements of data and code availability are available at https://doi.org/10.1038/s41567-023-02053-z.

https://doi.org/10.1038/s41567-023-02053-z

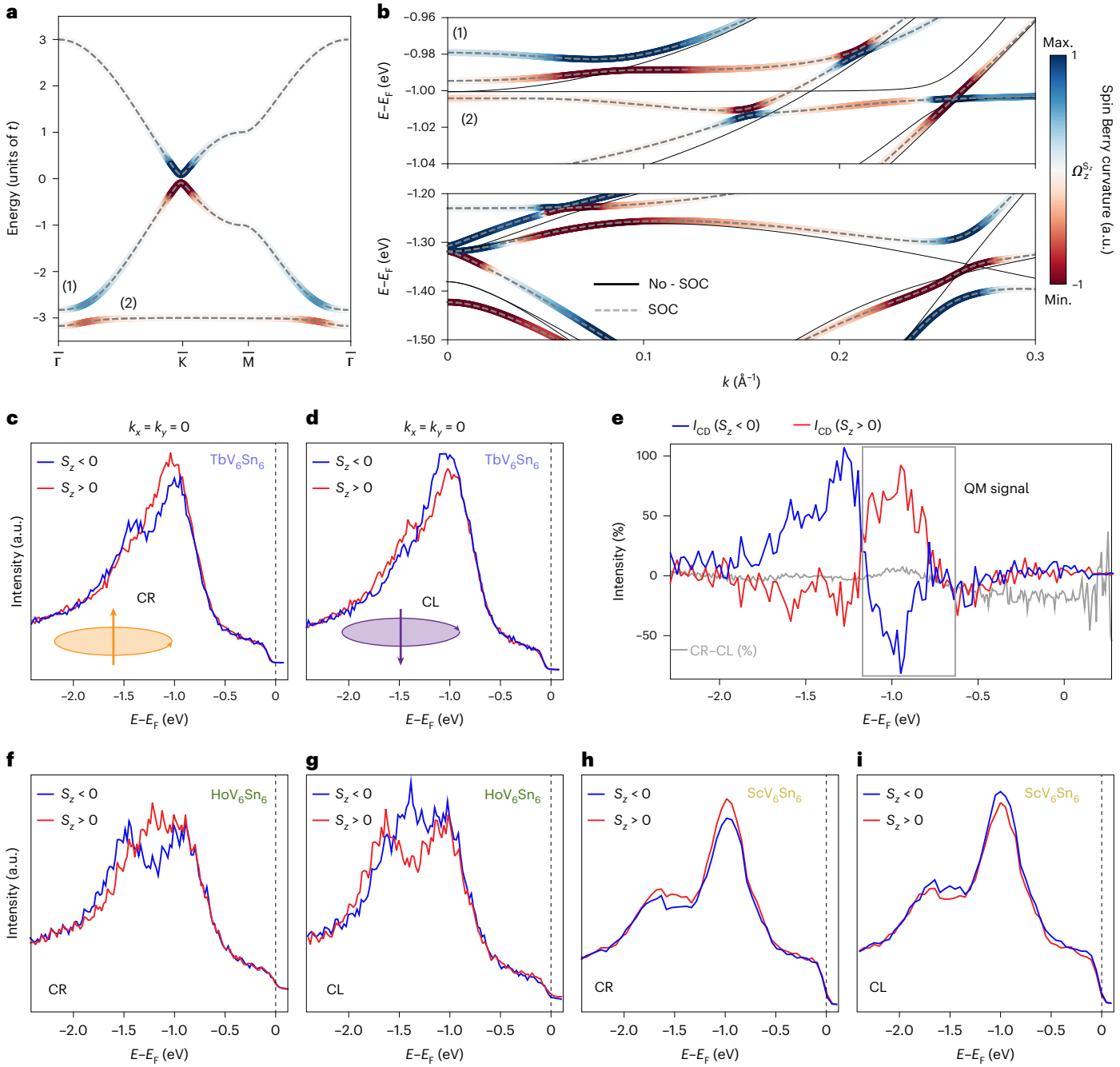

Fig. 4 | Topology of the flat band region. a, Band structure of a first-nearest-neighbour tight-binding model on the kagome lattice with SOC. The colour highlights the finite contribution from the spin Berry curvature $\Omega_z^{S_z}(\mathbf{k})$ around the SOC-induced gaps formed by bands (1) and (2). **b**, Same as **a** but for a realistic first-principles tight-binding model of TbV_6Sn_6 around the flat band region (top panel) and at slightly higher binding energies (bottom panel). **c**,**d**, Circular right (CR) (**c**) and circular left (CL) (**d**) spin-ARPES energy distribution curves, collected for the spin-↑ ($S_z > 0$, red) and spin-↓ ($S_z < 0$, blue) channels. The energy distribution curves have been collected at the centre of the BZ with the light entirely in the sample's mirror plane. Under these conditions, the geometrical contribution coming from the CD can be safely excluded. **e**, Extracted spin polarization for the CD (I_{CD} for $S_z<0$ and $S_z>0$), showing a strong and finite contribution for the quadratic minimum around −1 eV as high as approximately ±90%, as well as at higher binding energies. In grey, we also report the percentage contribution of the CD (CR − CL) for spin-integrated ARPES, showing fluctuations of the maximum ± 8% in the region of interest. **f**–**i**, Same as **c**,**d** for HoV_6Sn_6 (**f**,**g**) and ScV_6Sn_6 (**h**,**i**).

References

1. Balents, L. Spin liquids in frustrated magnets. *Nature* **464**, 199–208 (2010).
2. Guo, H.-M. & Franz, M. Topological insulator on the kagome lattice. *Phys. Rev. B* **80**, 113102 (2009).
3. Mazin, I. I. et al. Theoretical prediction of a strongly correlated dirac metal. *Nat. Commun.* **5**, 4261 (2014).
4. Kiesel, M. L. & Thomale, R. Sublattice interference in the kagome hubbard model. *Phys. Rev. B* **86**, 121105 (2012).
5. Kiesel, M. L., Platt, C. & Thomale, R. Unconventional fermi surface instabilities in the kagome hubbard model. *Phys. Rev. Lett.* **110**, 126405 (2013).
6. Di Sante, D. et al. Turbulent hydrodynamics in strongly correlated kagome metals. *Nat. Commun.* **11**, 3997 (2020).

7. Ortiz, B. R. et al. CsV_3Sb_5: A Z_2 topological kagome metal with a superconducting ground state. *Phys. Rev. Lett.* **125**, 247002 (2020).
8. Wu, X. et al. Nature of unconventional pairing in the kagome superconductors AV_3Sb_5 (a=K, Rb, Cs). *Phys. Rev. Lett.* **127**, 177001 (2021).
9. Neupert, T., Denner, M. M., Yin, J.-X., Thomale, R. & Hasan, M. Z. Charge order and superconductivity in kagome materials. *Nat. Phys.* **18**, 137–143 (2022).
10. Kang, M. et al. Topological flat bands in frustrated kagome lattice CoSn. *Nat. Commun.* **11**, 4004 (2020).
11. Kang, M. et al. Dirac fermions and flat bands in the ideal kagome metal FeSn. *Nat. Mater.* **19**, 163–169 (2020).
12. Lin, Z. et al. Flatbands and emergent ferromagnetic ordering in Fe_3Sn_2 kagome lattices. *Phys. Rev. Lett.* **121**, 096401 (2018).
13. Ye, L. et al. de haas-van alphen effect of correlated dirac states in kagome metal Fe_3Sn_2. *Nat. Commun.* **10**, 4870 (2019).
14. Frassineti, J. et al. Microscopic nature of the charge-density wave in the kagome superconductor RbV_3Sb_5. *Phys. Rev. Res.* **5**, L012017 (2023).
15. Pokharel, G. et al. Electronic properties of the topological kagome metals YV_6Sn_6 and GdV_6Sn_6. *Phys. Rev. B* **104**, 235139 (2021).
16. Hu, Y. et al. Tunable topological dirac surface states and van hove singularities in kagome metal GdV_6Sn_6. *Sci. Adv.* **8**, eadd2024 (2022).
17. Mielke, A. Ferromagnetism in the hubbard model on line graphs and further considerations. *J. Phys. A: Math. Gen.* **24**, 3311–3321 (1991).
18. Tang, E., Mei, J.-W. & Wen, X.-G. High-temperature fractional quantum hall states. *Phys. Rev. Lett.* **106**, 236802 (2011).
19. Rhim, J.-W., Kim, K. & Yang, B.-J. Quantum distance and anomalous landau levels of flat bands. *Nature* **584**, 59–63 (2020).
20. Weeks, C. & Franz, M. Flat bands with nontrivial topology in three dimensions. *Phys. Rev. B* **85**, 041104 (2012).
21. Gao, Z. & Lan, Z. Flat bands and $\mathbb{Z}_2$ topological phases in a non-abelian kagome lattice. *Phys. Rev. B* **102**, 245133 (2020).
22. Nakai, H. & Hotta, C. Perfect flat band with chirality and charge ordering out of strong spin-orbit interaction. *Nat. Commun.* **13**, 579 (2022).
23. Yan, Z. & Wan, S. Topological phases, topological flat bands, and topological excitations in a one-dimensional dimerized lattice with spin-orbit coupling. *EPL (Europhys. Lett.)* **107**, 47007 (2014).
24. Crasto de Lima, F., Ferreira, G. J. & Miwa, R. H. Topological flat band, dirac fermions and quantum spin Hall phase in 2d archimedean lattices. *Phys. Chem. Chem. Phys.* **21**, 22344–22350 (2019).
25. He, Q. L., Hughes, T. L., Armitage, N. P., Tokura, Y. & Wang, K. L. Topological spintronics and magnetoelectronics. *Nat. Mater.* **21**, 15–23 (2022).
26. Šmejkal, L., Mokrousov, Y., Yan, B. & MacDonald, A. H. Topological antiferromagnetic spintronics. *Nat. Phys.* **14**, 242–251 (2018).
27. He, M., Sun, H. & He, Q. L. Topological insulator: spintronics and quantum computations. *Front. Phys.* **14**, 43401 (2019).
28. Alam, S., Hossain, M. S. & Aziz, A. A non-volatile cryogenic random-access memory based on the quantum anomalous Hall effect. *Sci. Rep.* **11**, 7892 (2021).
29. Zhang, X. et al. Wearable non-volatile memory devices based on topological insulator Bi_2Se_3/Pt fibers. *Appl. Phys. Lett.* **107**, 103109 (2015).
30. Li, M. et al. Dirac cone, flat band and saddle point in kagome magnet YV_6Sn_6. *Nat. Commun.* **12**, 3129 (2021).
31. Chen, D. et al. Large anomalous Hall effect in the kagome ferromagnet $LiMn_6Sn_6$. *Phys. Rev. B* **103**, 144410 (2021).
32. Sun, Z. et al. Observation of topological flat bands in the kagome semiconductor Nb_3Cl_8. *Nano Lett.* **22**, 4596–4602 (2022).
33. Li, Z. et al. Realization of flat band with possible nontrivial topology in electronic kagome lattice. *Sci. Adv.* **4**, eaau4511 (2018).
34. Huang, H. et al. Flat-band-induced anomalous anisotropic charge transport and orbital magnetism in kagome metal CoSn. *Phys. Rev. Lett.* **128**, 096601 (2022).
35. Liu, Z. et al. Orbital-selective dirac fermions and extremely flat bands in frustrated kagome-lattice metal CoSn. *Nat. Commun.* **11**, 4002 (2020).
36. Ye, L. et al. Massive dirac fermions in a ferromagnetic kagome metal. *Nature* **555**, 638–642 (2018).
37. Peng, S. et al. Realizing kagome band structure in two-dimensional kagome surface states of RV_6Sn_6(R=Gd,Ho). *Phys. Rev. Lett.* **127**, 266401 (2021).
38. Yin, J.-X. et al. Negative flat band magnetism in a spin–orbit-coupled correlated kagome magnet. *Nat. Phys.* **15**, 443–448 (2019).
39. Arachchige, H. W. S. et al. Charge density wave in kagome lattice intermetallic ScV_6Sn_6. *Phys. Rev. Lett.* **129**, 216402 (2022).
40. Teng, X. et al. Discovery of charge density wave in a correlated kagome lattice antiferromagnet. *Nature* **609**, 490–495 (2022).
41. Fläschner, N. et al. Experimental reconstruction of the berry curvature in a floquet bloch band. *Science* **352**, 1091–1094 (2016).
42. Kruchkov, A. Quantum geometry, flat chern bands, and wannier orbital quantization. *Phys. Rev. B* **105**, L241102 (2022).
43. Ishikawa, H., Yajima, T., Kawamura, M., Mitamura, H. & Kindo, K. GdV_6Sn_6: a multi-carrier metal with non-magnetic 3d-electron kagome bands and 4f-electron magnetism. *J. Phys. Soc. Jpn* **90**, 124704 (2021).
44. Rosenberg, E. et al. Uniaxial ferromagnetism in the kagome metal TbV_6Sn_6. *Phys. Rev. B* **106**, 115139 (2022).
45. Fu, L. & Kane, C. L. Topological insulators with inversion symmetry. *Phys. Rev. B* **76**, 045302 (2007).
46. Lima, L. Spin transport in the two-dimensional antiferromagnet on kagome lattice. *J. Magn. Magn. Mater.* **561**, 169704 (2022).
47. Yang, S.-Y. et al. Giant, unconventional anomalous Hall effect in the metallic frustrated magnet candidate, KV_3Sb_5. *Sci. Adv.* **6**, eabb6003 (2020).
48. Zeng, H. et al. Large anomalous Hall effect in kagomé ferrimagnetic HoV_6Sn_6 single crystal. *J. Alloys Compd* **899**, 163356 (2022).
49. Liu, E. et al. Giant anomalous Hall effect in a ferromagnetic kagome-lattice semimetal. *Nat. Phys.* **14**, 1125–1131 (2018).
50. Owerre, S. A. Topological thermal Hall effect in frustrated kagome antiferromagnets. *Phys. Rev. B* **95**, 014422 (2017).
51. van Heumen, E. Kagome lattices with chiral charge density. *Nat. Mater.* **20**, 1308–1309 (2021).
52. Bolens, A. & Nagaosa, N. Topological states on the breathing kagome lattice. *Phys. Rev. B* **99**, 165141 (2019).
53. Bergman, D. L., Wu, C. & Balents, L. Band touching from real-space topology in frustrated hopping models. *Phys. Rev. B* **78**, 125104 (2008).
54. Roychowdhury, K., Attig, J., Trebst, S. & Lawler, M. J. Supersymmetry on the lattice: geometry, topology, and spin liquids. Preprint at *arXiv* https://doi.org/10.48550/arXiv.2207.09475 (2022).
55. Schüler, M. et al. Local Berry curvature signatures in dichroic angle-resolved photoelectron spectroscopy from two-dimensional materials. *Sci. Adv.* **6**, eaay2730 (2020).
56. Ünzelmann, M. et al. Momentum-space signatures of berry flux monopoles in the weyl semimetal taas. *Nat. Commun.* **12**, 3650 (2021).
57. Cho, S. et al. Studying local berry curvature in 2H-WSe_2 by circular dichroism photoemission utilizing crystal mirror plane. *Sci. Rep.* **11**, 1684 (2021).

58. Kang, M. et al. Twofold van hove singularity and origin of charge order in topological kagome superconductor CsV_3Sb_5. *Nat. Phys.* **18**, 301–308 (2022).
59. Consiglio, A. et al. Van hove tuning of AV_3Sb_5 kagome metals under pressure and strain. *Phys. Rev. B* **105**, 165146 (2022).

Methods

Experimental details

Single crystals of XV_6Sn_6 (Tb, Sc and Ho) were grown using a flux-based growth technique as reported in ref. 60. X (chunk, 99.9%), V (pieces, 99.7%) and Sn (shot, 99.99%) were loaded inside an alumina crucible with the molar ratio of 1:6:20 and then heated at 1,125 °C for 12 h. Then, the mixture was slowly cooled to 780 °C at a rate of 2 °C h^{-1}. Thin plate-like single crystals were separated from the excess Sn flux by centrifugation at 780 °C. The samples were cleaved in ultrahigh vacuum at a pressure of 1×10^{-10} mbar. The spin-ARPES data were acquired at the APE-LE end station (Trieste) using a VLEED-DA30 hemispherical analyser. The energy and momentum resolutions were better than 12 meV and 0.02 $Å^{-1}$, respectively. The temperature of the measurements was kept constant throughout the data acquisitions (16 K and 77 K), above the magnetic transition of the system (<5 K). Both linear and circular polarized light was used to collect the data from the APE undulator of the synchrotron radiation source ELETTRA (Trieste).

Theoretical details

We employed first-principles calculations based on the DFT as implemented in the Vienna ab-initio simulation package[61], within the projector-augmented plane-wave method[62]. The generalized gradient approximation as parametrized by the Perdew-Burke-Ernzerhof functional for the exchange-correlation potential was used[63] by expanding the Kohn–Sham wave functions into plane waves up to an energy cutoff of 400 eV. We sample the BZ on an $12 \times 12 \times 6$ regular mesh by including SOC self-consistently. For the calculation of the surface spectral function, the Kohn–Sham wave functions were projected onto a Tb *d*, V *d* and Sn *s*, *p*-type basis. The calculation of the spin Berry curvature requires a Wannier Hamiltonian where the lattice symmetries are properly enforced. For this reason, we used the full-potential local-orbital code[64], v.21.00-61 (https://www.FPLO.de/). The spin Berry curvature for band n is then defined as

$$\Omega^{z}_{xy}(\mathbf{k}) = \sum_{E_n > E_{m \neq n}} \frac{\langle n| v^{z}_{s,x} |m\rangle \langle m| v_y |n\rangle (x \leftrightarrow y)}{(E_{n\mathbf{k}} - E_{m\mathbf{k}})^2}, \quad (1)$$

with the spin operator σ_z and velocity operator $v_i = \frac{1}{\hbar}\partial H/\partial k_i$ ($i = x, y$). $|n\mathbf{k}\rangle$ is the eigenvector of the Hamiltonian H with the eigenvalue $E_{n\mathbf{k}}$. Equation (1) is computed by using our in-house post-wan library (Code availability).

Data availability

Source data are provided with this paper and are also available at https://doi.org/10.5281/zenodo.7787937.

Code availability

Our in-house post-wan library used to compute Berry curvature-related quantities can be downloaded from https://github.com/philipp-eck/post_wan.

References

60. Ganesh, P. et al. Highly anisotropic magnetism in the vanadium-based kagome metal TbV_6Sn_6. *Phys. Rev. Mater.* **6**, 104202 (2022).
61. Kresse, G. & Furthmüller, J. Efficient iterative schemes for ab initio total-energy calculations using a plane-wave basis set. *Phys. Rev. B* **54**, 11169 (1996).
62. Blöchl, P. E. Projector augmented-wave method. *Phys. Rev. B* **50**, 17953–17979 (1994).
63. Perdew, J. P., Burke, K. & Ernzerhof, M. Generalized gradient approximation made simple. *Phys. Rev. Lett.* **77**, 3865 (1996).
64. Koepernik, K. & Eschrig, H. Full-potential nonorthogonal local-orbital minimum-basis band-structure scheme. *Phys. Rev. B* **59**, 1743 (1999).

Acknowledgements

We are grateful to O. Janson and T. Schwemmer for insightful discussions. The research leading to these results has received funding from the European Union's Horizon 2020 research and innovation programme under the Marie Skłodowska-Curie Grant Agreement No. 897276 (D.D.S.). G.S., R.T., P.E., S.E. and A.C. are grateful for funding support from the Deutsche Forschungsgemeinschaft (DFG, German Research Foundation) under Germany's Excellence Strategy through the Würzburg-Dresden Cluster of Excellence on Complexity and Topology in Quantum Matter ct.qmat (EXC 2147, Project ID 390858490), through QUAST FOR 5249 (Project No. 449872909) as well as through the Collaborative Research Center SFB 1170 ToCoTronics (Project ID 258499086). This work has been performed in the framework of the Nanoscience Foundry and Fine Analysis (NFFA-MUR Italy Progetti Internazionali) facility (G. Panaccione and G.R.). S.D.W. and G. Pokharel acknowledge support via the UC Santa Barbara NSF Quantum Foundry funded via the Q-AMASE-i programme under award no. DMR-1906325. C.B. and P.D.C.K. gratefully acknowledge support from The Leverhulme Trust through project no. RL-2016-006. F.M. greatly acknowledges the Seal of Excellence action of PNRR (Piano Nazionale di Ripresa e Resilienza), no. SOE_0000068. I.Z. acknowledges support from the US Department of Energy Early Career award DE-SC0020130. We gratefully acknowledge the Gauss Centre for Supercomputing e.V. (https://www.gauss-centre.eu) for funding this project by providing computing time on the GCS Supercomputer SuperMUC-NG at Leibniz Supercomputing Centre (https://www.lrz.de). The Flatiron Institute is a division of the Simons Foundation.

Author contributions

D.D.S, G. Panaccione, G.S. and F.M. conceived and designed the project. G. Pokharel and S.D.W. grew the crystals. F.M., C.B. and P.C. carried out the spin-ARPES and ARPES measurements. D.D.S., G.S., S.E., P.E. and A.C. performed the numerical calculations. All the authors participated in the discussion and contributed to the writing of the manuscript.

Competing interests

The authors declare no competing interests.

Additional information

Supplementary information The online version contains supplementary material available at https://doi.org/10.1038/s41567-023-02053-z.

Correspondence and requests for materials should be addressed to Domenico Di Sante, Giorgio Sangiovanni, Giancarlo Panaccione or Federico Mazzola.

Peer review information *Nature Physics* thanks the anonymous reviewers for their contribution to the peer review of this work.